Monthly Notices
of the
ROYAL ASTRONOMICAL SOCIETY

MNRAS **453,** 2–13 (2015) doi:10.1093/mnras/stv1561

Non-virialized clusters for detection of dark energy–dark matter interaction

M. Le Delliou,[1,2⋆] R. J. F. Marcondes,[2⋆] G. B. Lima Neto[3] and E. Abdalla[2]

[1]*Instituto de Física Teórica, Universidade Estadual Paulista, R. Dr. Bento Teobaldo Ferraz, 271 - Bloco II, Barra-Funda CEP 01140-070, São Paulo, SP, Brazil*

[2]*Departamento de Física Matemática, Instituto de Física, Universidade de São Paulo, Rua do Matão Travessa R Nr.187 CEP 05508-090, São Paulo/SP, Brazil*

[3]*Instituto de Astronomia, Geofísica e Ciências Atmosféricas, Universidade de São Paulo, Rua do Matão 1226, Cidade Universitária, CEP 05508-090, São Paulo/SP, Brazil*

Accepted 2015 July 10. Received 2015 June 13; in original form 2014 November 20

ABSTRACT

The observation of galaxy and gas distributions, as well as cosmological simulations in a ΛCDM cold dark matter universe, suggests that clusters of galaxies are still accreting mass and are not expected to be in equilibrium. In this work, we investigate the possibility to evaluate the departure from virial equilibrium in order to detect, in that balance, effects from a dark matter–dark energy interaction. We continue, from previous works, using a simple model of interacting dark sector, the Layzer–Irvine equation for dynamical virial evolution, and employ optical observations in order to obtain the mass profiles through weak-lensing and X-ray observations giving the intracluster gas temperatures. Through a Monte Carlo method, we generate, for a set of clusters, measurements of observed virial ratios, interaction strength, rest virial ratio and departure from equilibrium factors. We found a compounded interaction strength of $-1.99^{+2.56}_{-16.00}$, compatible with no interaction, but also a compounded rest virial ratio of -0.79 ± 0.13, which would entail a 2σ detection. We confirm quantitatively that clusters of galaxies are out of equilibrium but further investigation is needed to constrain a possible interaction in the dark sector.

Key words: Gravitation – Galaxies: clusters: general – Cosmology: theory – dark energy – dark matter – large-scale structure of Universe – X-rays: galaxies: clusters.

1 INTRODUCTION

The surprising result of cosmological accelerated expansion, discovered at first from supernovae data (Perlmutter et al. 1998), and the long sought Dark Matter (DM) seen around clumped matter (Zwicky 1933, 1937), found their importance combined and confirmed by the results of cosmological microwave background observations (Planck Collaboration XVI 2014b). This leads to the fair confidence on the existence of a dark sector, composed by an inert cold dark matter accounting for ∼27 per cent of the Universe and a rather mysterious dark energy (DE), accelerating the cosmos, accounting for another ∼68 per cent (Planck Collaboration XVI 2014b).

The nature of these components is largely unknown. Several candidates for DM appeared in the literature, with no preference from observations. For DE, a cosmological constant (de Sitter space type) is the usual observationally preferred choice and forms the basis of the so-called standard, or concordance, cosmology (Bennett et al. 2013; Hinshaw et al. 2013; Planck Collaboration III 2013; Planck Collaboration I 2014a).

However, such cosmological constant is an awful choice from the theoretical point of view: it has been argued that it differs by 120 orders of magnitude from a reasonable field theory estimation (Weinberg 1989, 2008). From observations, the fact that its energy density is of the same order of magnitude today as the DM is a mystery: both depend on cosmological time in a completely different way, leading to the so-called coincidence problem (Amendola 2000; Tocchini-Valentini & Amendola 2002; Zimdahl & Pavón 2001, 2003).

From the observational standpoint it turns out to be very difficult to distinguish a clear departure from the standard cosmological model. Indeed, cosmology is reasonably well described by a positive cosmological constant in a framework of a set of Einstein equations. A redshift-dependent equation of state of DE is possible but the error bars obtained from observations so far are still consistent (to one or two standard deviations) with the standard cosmological model, although such model is theoretically unsatisfactory as discussed above.

On the contrary, dynamic DE was theoretically introduced in attempts to solve the fine tuning and coincidence problems

⋆ E-mail: delliou@ift.unesp.br (MLD); mrafael@if.usp.br (RJFM)

described above (Caldwell, Dave & Steinhardt 1998; Copeland, Liddle & Wands 1998; Zlatev, Wang & Steinhardt 1999), first using quintessence models such as (Ratra & Peebles 1988; Wetterich 1988), then opening to other models, such as *k*-essence (Armendariz-Picon, Mukhanov & Steinhardt 2001) or the generalized Chaplygin gas (Bento, Bertolami & Sen 2002; Bilić, Tupper & Viollier 2002). In this framework, it was pointed out that, since the main components of the universe in the standard cosmological models are yet unknown, that dark sector interactions, that is the non-minimal coupling between DM and DE, would be the most natural model to consider (Amendola 2000). Such models are not ruled out by observations (Pettorino et al. 2012; Pettorino 2013).

One possibility that has been put forward a few years ago is that interaction can spoil the virial theorem (or else the Layzer–Irvine equation in General Relativity) (Bertolami, Gil Pedro & Le Delliou 2007; Le Delliou, Bertolami & Gil Pedro 2007; Bertolami, Gil Pedro & Le Delliou 2008, 2009, 2012). Such a possibility has been checked by different groups (Abdalla et al. 2009; Abdalla, Abramo & de Souza 2010; He et al. 2010) and the results are still not completely settled, although they all point towards the existence of an interacting dark sector. Indeed, using a series of data from clusters, we can infer, under some not too severe conditions, whether DE can play the role of a hidden external driving force by means of the dark sector interaction and thus apparently spoil the virial theorem leaving a trace of the would-be interaction. In such a case, some limits on the interaction can be obtained.

In this paper, we consider the virial condition and investigate if it can be clearly imposed observationally, by enquiring into cluster data and their corresponding observations in the optical and X-ray bands. These bands were chosen because, from deep optical imaging it is possible to derive the total mass distribution through weak-lensing effect of background galaxies, and from X-ray observations we can determine the density and temperature of the intracluster gas, which traces the cluster gravitational potential well.

In previous papers, deviations from the virial theorem, as described in the Layzer–Irvine equation, were searched in very relaxed clusters (Bertolami et al. 2007, 2008, 2009, 2012; Le Delliou et al. 2007) or in large sets of clusters (Abdalla et al. 2009, 2010; He et al. 2010). In Bertolami et al. (2007), optical (weak lensing) and X-rays data were used to provide the first hint of a detection of a putative violation of the Equivalence Principle in the virial state of Abell 586. Subsequent works aimed at refining the method on Abell 586 (Le Delliou et al. 2007; Bertolami et al. 2008, 2009) and introduced another relaxed cluster candidate (Abell 1689; Bertolami et al. 2012). In Abdalla et al. (2009), optical and X-ray data were compared and a hint of systematic bias in the estimation of masses, if the usual virial conditions are employed, was found. In a subsequent paper (Abdalla et al. 2010), the work was extended to a larger set of clusters. In both cases, it was argued that such signals might point to new physics to be uncovered and more specifically to a correction of the virial theorem due to a would-be interaction of DM with a hidden sector, i.e. DE, driving the system away from the virial equilibrium.

In this work, we address some of these issues raised previously, digging into the internal structure of the clusters, in order to find, in a very direct way, not only the kinetic versus potential energy – the virial ratio – from each system (cluster), but also to use the full dynamics of the Layzer–Irvine equation, including the same fluid model for DM and DE as used in previous works, in order to extract an assessment of the departure from self-gravitating equilibrium.

The next section describes the techniques used for extracting relevant dynamical quantities from the data. Section 3 compiles the relevant data and summarizes their treatment. The results obtained are given in Section 4, and we conclude with a discussion in Section 5. We adopt whenever necessary the standard flat ΛCDM parameters: $\Omega_{\rm M} = 0.32$ for the Matter density parameter, $\Omega_{\rm DE} = 0.68$ for the DE parameter and Hubble constant $H_0 = 67.0\,{\rm km\,s^{-1}\,Mpc^{-1}}$, according to the best-fitting parameters from *Planck* temperature combined with *WMAP* polarization at low multipoles (Planck Collaboration XVI 2014b).

2 VIRIAL RATIO AND DEPARTURE FROM EQUILIBRIUM FOR NON-VIRIALIZED CLUSTERS

In Abdalla et al. (2009), a model of interaction involving the coupling of both DM and DE was introduced for which the Layzer–Irvine equation was deduced. We adopt a form, in what follows, that is inspired by such model.

2.1 The Layzer–Irvine model with interaction

The Layzer–Irvine equation (Peebles 1993) is a model of dynamical virial balance where the disturbance is simplified in the expansion of the background universe.

2.1.1 The interaction model

Following Abdalla et al. (2009, 2010) and He et al. (2010), we model the DM–DE interaction via a heat flux between the two species, themselves treated as fluids with constant equation-of-state parameters, in their partial Bianchi identities in a Friedmann–Lemaître–Robertson–Walker (FLRW) background model

$$\dot{\rho}_{\rm DM} + 3H\rho_{\rm DM} = 3H\left(\xi_1\rho_{\rm DM} + \xi_2\rho_{\rm DE}\right), \tag{1}$$

$$\dot{\rho}_{\rm DE} + 3H\rho_{\rm DE}(1+\omega_{\rm DE}) = -3H\left(\xi_1\rho_{\rm DM} + \xi_2\rho_{\rm DE}\right). \tag{2}$$

Here we have used the indices to refer to species, the couplings ξ_1 and ξ_2, hereafter interaction strengths, the densities denoted by ρ_x while their corresponding equation of state reads ω_x and the FLRW Hubble parameter H. In what follows we shall simplify the interaction by choosing $\xi_1 = \frac{\xi}{18}$ and $\xi_2 = -\frac{\xi}{6}\frac{\rho_{\rm DM}}{\rho_{\rm DE}}$ and writing $\rho_{\rm DM} = \rho$, yielding a positive flux $\frac{\xi}{3}H\rho$ towards DE when all terms are positive.

The resulting Layzer–Irvine equation for the DM component (He et al. 2010), referring to its kinetic energy density with ρ_K while its potential energy density writes ρ_W, reads

$$\dot{\rho} + H\left[\left(2-\frac{\xi}{3}\right)\rho_K + \left(1-\frac{\xi}{3}\right)\rho_W\right] = 0. \tag{3}$$

In case of equilibrium, the time derivative vanishes and yield the interacting virial balance as

$$\frac{\rho_K}{\rho_W} = -\frac{1-\frac{\xi}{3}}{2-\frac{\xi}{3}}. \tag{4}$$

However, in this work, we want to take into account departures from equilibrium.

Note, that certainty of convergence of the energy density towards equilibrium, together with other magnitude restriction considerations (e.g. He, Wang & Abdalla 2011), prescribes from equation (3) to exclude values of ξ higher than 3.

2.1.2 *The Non-Virialized model*

In order to simplify the calculation, we approximate the departure of ρ_K from balance as proportional to the departure of ρ_W and introduce equation (4) into (3) to get

$$\left[1-\frac{1-\frac{\xi}{3}}{2-\frac{\xi}{3}}\right]\dot{\rho}_W = -H\left[\left(2-\frac{\xi}{3}\right)\rho_K+\left(1-\frac{\xi}{3}\right)\rho_W\right] \quad (5)$$

so

$$\frac{\rho_K}{\rho_W} = -\frac{1-\frac{\xi}{3}}{2-\frac{\xi}{3}} - \frac{1}{\left(2-\frac{\xi}{3}\right)^2}\frac{\dot{\rho}_W}{H\rho_W}. \quad (6)$$

Here we find that the true virial balance (4) is corrected by a term we call departure from equilibrium (DfE). For our approximation (4) to remain valid, the DM halo has to be close to virial balance, so we have to check that

$$\left|\frac{\dot{\rho}_W}{H\rho_W}\right| \ll \left(2-\frac{\xi}{3}\right)\left(1-\frac{\xi}{3}\right). \quad (7)$$

In that case, ρ_K, ρ_W, $\dot{\rho}_W$ and H being observable, we can solve equation (6) for the coupling and obtain

$$\xi = 3\left(\frac{3+4\frac{\rho_K}{\rho_W}-\sqrt{1-\frac{4\dot{\rho}_W}{H\rho_W}\left(1+\frac{\rho_K}{\rho_W}\right)}}{2\left(1+\frac{\rho_K}{\rho_W}\right)}\right). \quad (8)$$

The expression verifies the classical, non-interacting and virialized, result: $\xi = 0$ for $\dot{\rho}_W = 0$ and $\frac{\rho_K}{\rho_W} = -\frac{1}{2}$. Note that this equation is singular at $\frac{\rho_K}{\rho_W} = -1$, which originates in the left-hand side of equation (5) and corresponds to infinite ξ.

Note that this method sums all possible dynamical sources of deviation from the stationary true virial balance into this DfE factor, including sources such as simulations imperfectly stationary states caused by finite integration time and/or numerical noise and, for observed clusters, the possibility of recent merger events kinetic remnants, inflows from neighbouring clusters or baryonic sources of kinetic injection in the cluster (supernova feedback, baryons–DM dynamical friction) (Kravtsov & Borgani 2012). The evaluation of any sources of deviations of the real virial balance from the virial theorem classical value (Binney & Tremaine 2008) are encoded in our simple model of DM–DE interaction as the presently conceived source. Thus far, no other source of deviation claims to have an effect that would not vanish at real equilibrium. We are henceforth justified in considering this evaluation as a handle on possible interaction and its subsequent violation of the Equivalence Principle between baryons and DM. We note however that given the simplifications, this work should be considered as a proof of concept for such an evaluation on unbalanced clusters.

We now need to evaluate ρ_K, ρ_W, $\dot{\rho}_W$ and H from cluster observations. However, as we will see in Section 2.2.3, the factor $\frac{\dot{\rho}_W}{H\rho_W}$ in the DfE is not a pure observable and depends on ξ.

2.2 The evaluation from clusters

As will be seen in Section 3, for each cluster we essentially have access to the total mass distribution through weak-lensing observations given in the form of Navarro, Frenk and White (NFW) profile parameter fits, and hence can derive its potential energy, and to the evaluation of the cluster's kinetic state through its X-ray temperature, that we can then transform into an evaluation of its kinetic energy. In what follows, we provide the framework to make contact between such observables and the theoretical scheme we have presented above.

2.2.1 *The NFW density and weak-lensing mass*

The NFW density profile (Navarro, Frenk & White 1996) found in N-body simulations is commonly used to fit observed clusters in order to parametrize their mass distribution. The classical form of the NFW profile involves the radius of logarithmic slope change r_0 and the corresponding density ρ_0. Assuming the virial radius of clusters lies at a density contrast of about 200 above the background density for clusters, the NFW concentration parameter can be defined as $c = \frac{r_{200}}{r_0}$. Moreover, the profile's integration yields a mass profile from which M_{200} can be extracted. In terms of c, r_{200} and M_{200}, the mass and density profiles read

$$M = \frac{M_{200}}{\ln(1+c)-\frac{c}{1+c}}\left[\ln\left(1+c\frac{r}{r_{200}}\right)-\frac{c\frac{r}{r_{200}}}{1+c\frac{r}{r_{200}}}\right], \quad (9)$$

$$\rho = \frac{M_{200}}{4\pi r_{200}^3\left[\ln(1+c)-\frac{c}{1+c}\right]}\frac{c^2}{\frac{r}{r_{200}}\left(1+c\frac{r}{r_{200}}\right)^2}. \quad (10)$$

The parameter describing the best-fitting NFW profile, c and r_{200} (or M_{200}), can be obtained from the mass reconstruction technique, which requires deep imaging with small point spread function (PSF) that can detect the weak-lensing effect.

2.2.2 *The potential and kinetic energy density evaluations*

With the previously presented NFW mass profile, the density of potential energy is straightforwardly integrated

$$\rho_W \equiv -\frac{4\pi}{\frac{4}{3}\pi r_{200}^3}\int_0^{r_{200}}\frac{\rho(r)GM(r)}{r}r^2\,\mathrm{d}r = -\frac{3GM_{200}^2}{4\pi r_{200}^4 f_c}, \quad (11)$$

with

$$f_c \equiv \frac{(1+c)\left[\ln(1+c)-c(1+c)^{-1}\right]^2}{c\left[\frac{1}{2}\left\{(1+c)-(1+c)^{-1}\right\}-\ln(1+c)\right]}. \quad (12)$$

On the other hand, in order to evaluate the kinetic state of the cluster, we use published X-rays observations, where we just need to obtain the X-ray temperature to get the equipartition formula

$$\rho_K = \frac{3}{2}N\frac{k_{\mathrm{B}}T_X}{V} = \frac{9}{8\pi}\frac{M_{200}}{r_{200}^3}\frac{k_{\mathrm{B}}T_X}{\mu m_{\mathrm{H}}}, \quad (13)$$

gauging the equivalent number of particles from the total mass given by weak-lensing $\frac{M_{200}}{\mu m_{\mathrm{H}}}$, where μ is the mean molecular mass in the intracluster gas and m_{H} is the mass of a proton. The advantage of this method, compared, say, to using the galaxy velocity dispersion or a scaling relation σ_X–T_X, as in Bertolami et al. (2007), Le Delliou et al. (2007) and Bertolami et al. (2008, 2009, 2012), is that we avoid the error from the scatter in the scaling relation. We are justified in evaluating the kinetic state of clusters through the single compounded temperature T_X, extracted from the X-ray flux of the whole r_{500} central region, as it already largely encompasses the turnaround of the temperature profile (Vikhlinin et al. 2005; Pratt et al. 2007; Moretti et al. 2011), and therefore represents well the total density averaged temperature (the so-called virial temperature).

At this point the virial ratio can be evaluated as

$$\frac{\rho_K}{\rho_W} = -\frac{3}{2}\frac{r_{200}}{GM_{200}}\frac{k_{\mathrm{B}}T_X}{\mu m_{\mathrm{H}}}f_c. \quad (14)$$

2.2.3 *The virial and departure from equilibrium evaluation*

The DfE factor can be rewritten as

$$-\frac{1}{\left(2-\frac{\xi}{3}\right)^2}\frac{\dot{\rho}_W}{H\rho_W} = -\frac{1}{\left(2-\frac{\xi}{3}\right)^2}\frac{\rho'_W}{H\rho_W}\dot{r}_{200}, \tag{15}$$

where we get from equation (11)

$$\frac{\mathrm{d}\ln(-\rho_W)}{\mathrm{d}r_{200}} = \frac{\rho'_W}{\rho_W} = \frac{cg_c-3}{r_{200}}, \tag{16}$$

with

$$g_c \equiv \frac{\ln(1+c)-c(1+c)^{-1}}{\frac{c}{2}(c+2)-(1+c)\ln(1+c)}. \tag{17}$$

Now remains to evaluate $\dot{r}_{200}$. We can define the kinetic density using a one-dimensional velocity dispersion, thus defining σ_X^2:

$$\rho_K = \frac{3}{2}\frac{M_{200}}{V}\sigma_X^2 \Rightarrow \sigma_X^2 = \frac{k_\mathrm{B}T_X}{\mu m_\mathrm{H}}. \tag{18}$$

We now define the theoretical average velocity dispersion the cluster would have if it were at virial equilibrium, adiabatically evolving from the current state (meaning keeping potential energy about constant)

$$\left(\frac{\rho_K}{\rho_W}\right)_\mathrm{th} = -\frac{1-\frac{\xi}{3}}{2-\frac{\xi}{3}} \quad \text{with} \quad \rho_{K\,\mathrm{th}} = \frac{3}{2}\frac{M_{200}}{V}v_\mathrm{th}^2 \tag{19}$$

$$\Leftrightarrow v_\mathrm{th}^2 = \frac{1}{3}\frac{6-2\xi}{6-\xi}\frac{GM_{200}}{f_c r_{200}}. \tag{20}$$

We can finally evaluate the time evolution of r_{200} by taking its difference with the velocity dispersion

$$\dot{r}_{200} = \sqrt{\sigma_X^2} - \sqrt{v_\mathrm{th}^2} = \sigma_X - v_\mathrm{th}, \tag{21}$$

we obtain

$$-\frac{\dot{\rho}_W}{H\left(2-\frac{\xi}{3}\right)^2\rho_W} = -\frac{1}{H\left(2-\frac{\xi}{3}\right)^2}\frac{(cg_c-3)}{r_{200}} \times\left(\sqrt{\frac{k_\mathrm{B}T_X}{\mu m_\mathrm{H}}} - \sqrt{\frac{1}{3}\frac{6-2\xi}{6-\xi}\frac{GM_{200}}{f_c r_{200}}}\right). \tag{22}$$

With this equation, we estimate the departure from equilibrium due to 'standard' dynamical sources (e.g. cluster collisions, AGN and supernova feedback, dynamical friction) combining observations and the DE model, leaving no room for degeneracy in the determination of ξ. The DfE presented here appears model dependent in its explicit reference to the interaction strength; however, the method can use any model we want that gives a definite shift to the virial balance.[1] In this case, decrease to negative values of ξ from 0, at fixed observations, would decrease the absolute value of clusters with kinetic velocity above their virial one and up to increase those of the opposite case.

[1]
$$\frac{\mathrm{VR}\,\dot{\rho}_W}{Hc_W(1+\mathrm{VR})\rho_W} = -\frac{\mathrm{VR}}{Hc_W(1+\mathrm{VR})}\frac{(cg_c-3)}{r_{200}} \times\left(\sqrt{\frac{k_\mathrm{B}T_X}{\mu m_\mathrm{H}}} - \sqrt{-\frac{2}{3}\mathrm{VR}\frac{GM_{200}}{f_c r_{200}}}\right), \tag{23}$$

where VR is the virial ratio and c_W is the potential coefficient in the Layzer–Irvine equation.

3 COMPUTATIONS OF THE VIRIAL RATIOS AND DEPARTURE FROM EQUILIBRIUM FOR A SET OF NON-VIRIALIZED CLUSTERS

Cosmologically interesting observations of clusters are produced in many surveys and studies such as Okabe et al. (2010) and Planck Collaboration III (2013). In order to maximize our sample, while being able to separately evaluate from observations the kinetic and potential energy states of each cluster, we have restricted inputs to weak-lensing NFW fit parameters (Navarro et al. 1996), X-ray-derived c_{500} NFW fits, and X-ray temperatures.

3.1 The sample

In order to try to minimize any systematics due to observational uncertainties, the clusters in our sample should present well determined X-ray gas temperature, as well as NFW profile fitted to the mass distribution obtained with weak-lensing observations.

Most of the 22 clusters in our sample come from Okabe et al. (2010). Their NFW profiles are described by best-fitting virial masses M_vir, concentration parameters c_vir and masses M_{200} estimated from this three-dimensional model fitting. Those are the Abell clusters A68, A115, A209, A267, A383, A521, A586, A611, A697, A1835, A2219, A2261, A2390, A2631 and also RX J1720.1+2638, RX J2129.6+0005, ZwCl 1454.8+2233 and ZwCl 1459.4+4240. Their weak-lensing data are shown in Table 1. We also include four more clusters from Planck Collaboration III (2013): A520, A963, A1914 and A2034 (data in Table 2). Weak-lensing masses M_{500} and best-fitting NFW concentration parameter c_{500} are given instead of M_vir, c_vir and M_{200} for these clusters. However, the error bars for c_{500} were estimated from the X-ray data, since they are not given by Planck Collaboration III (2013). The spectroscopically determined temperatures T_X are measured within r_{500} and are all given in Planck Collaboration III (2013), with the exceptions of A115

Table 1. Weak-lensing masses M_{200}, M_vir and concentration c_vir for the Okabe's clusters. Masses are in units of $h^{-1}10^{14}\,\mathrm{M}_\odot$.

Cluster	M_{200}	M_vir	c_vir
A68	$4.45^{+1.75}_{-1.35}$	$5.49^{+2.56}_{-1.81}$	$4.02^{+3.36}_{-1.82}$
A115	$4.24^{+2.60}_{-1.79}$	$5.36^{+4.08}_{-2.45}$	$3.69^{+5.03}_{-2.04}$
A209	$10.62^{+2.17}_{-1.81}$	$14.00^{+3.31}_{-2.60}$	$2.71^{+0.69}_{-0.60}$
A267	$3.23^{+0.82}_{-0.69}$	$3.85^{+1.08}_{-0.88}$	$6.00^{+2.11}_{-1.58}$
A383	$3.11^{+0.88}_{-0.69}$	$3.62^{+1.15}_{-0.86}$	$8.87^{+5.22}_{-3.05}$
A521	$4.58^{+1.00}_{-0.88}$	$5.85^{+1.45}_{-1.22}$	$3.06^{+1.01}_{-0.79}$
A586	$6.29^{+2.26}_{-1.69}$	$7.37^{+2.89}_{-2.08}$	$8.38^{+3.52}_{-2.52}$
A611	$5.47^{+1.31}_{-1.11}$	$6.65^{+1.75}_{-1.42}$	$4.23^{+1.77}_{-1.23}$
A697	$9.73^{+1.86}_{-1.61}$	$12.36^{+2.68}_{-2.21}$	$2.97^{+0.85}_{-0.69}$
A1835	$10.86^{+2.53}_{-2.08}$	$13.69^{+3.65}_{-2.86}$	$3.35^{+0.99}_{-0.79}$
A2219	$7.75^{+1.89}_{-1.60}$	$9.11^{+2.54}_{-2.06}$	$6.88^{+3.42}_{-2.16}$
A2261	$7.97^{+1.51}_{-1.31}$	$9.49^{+2.01}_{-1.69}$	$6.04^{+1.71}_{-1.31}$
A2390	$6.92^{+1.50}_{-1.29}$	$8.20^{+1.93}_{-1.63}$	$6.20^{+1.53}_{-1.28}$
A2631	$4.54^{+0.89}_{-0.78}$	$5.24^{+1.15}_{-0.98}$	$7.84^{+3.54}_{-2.28}$
RX J1720	$3.48^{+1.28}_{-0.99}$	$4.07^{+1.65}_{-1.22}$	$8.73^{+5.60}_{-3.08}$
RX J2129	$5.29^{+1.76}_{-1.38}$	$6.71^{+2.73}_{-1.96}$	$3.32^{+2.16}_{-1.34}$
ZwCl 1454	$2.80^{+1.39}_{-1.03}$	$3.45^{+2.02}_{-1.36}$	$4.01^{+3.44}_{-1.96}$
ZwCl 1459	$3.77^{+1.17}_{-0.98}$	$4.40^{+1.50}_{-1.20}$	$6.55^{+3.34}_{-2.18}$

Notes: Data from Okabe et al. (2010).

Table 2. Weak-lensing masses M_{500} and concentration c_{500} for the Planck Collaboration's clusters. Masses are in units of $10^{14}\,M_\odot$.

Cluster	M_{500}	c_{500}
A520	$4.1^{+1.1}_{-1.2}$	1.4 ± 0.6
A963	$4.2^{+0.9}_{-0.7}$	1.2 ± 0.2
A1914	$4.7^{+1.6}_{-1.9}$	2.0 ± 0.2
A2034	$5.1^{+2.1}_{-2.4}$	1.8 ± 0.3

Notes: Data from Planck Collaboration III (2013).

and A697 from Landry et al. (2013) and A611 from Kenneth et al. (2008). Uncertainties correspond to 1σ confidence level (C.L.). Errors in redshifts (see Table 3) are not specified but can be safely neglected compared to the errors in other quantities (the typical spectroscopic redshift error is around 1 per cent).

3.1.1 *Uniforming the NFW profiles*

To compute the potential energy, we use weak-lensing observational fittings of NFW profiles. These fittings, justified by the observers confidence in their reliability (Okabe et al. 2010; Ettori et al. 2013), are further vindicated by interacting DE models from simulations (e. g. Baldi et al. 2010; Carlesi et al. 2014) which all agree with the NFW shape.

Table 3. Redshift, temperature and compiled NFW parameters of the 22 galaxy clusters. Temperatures are given in keV and masses in units of $h^{-1}10^{14}\,M_\odot$.

Cluster	z	$k_B T_X$	M_{200}	c
A68	0.255	8.3 ± 0.3	$4.45^{+1.75}_{-1.35}$	$2.49^{+3.12}_{-1.65}$
A115	0.197	$8.9^{+0.6}_{-0.7}$	$4.24^{+2.60}_{-1.79}$	$1.86^{+3.52}_{-1.48}$
A209	0.206	6.6 ± 0.2	$10.62^{+2.17}_{-1.81}$	$1.90^{+0.81}_{-0.63}$
A267	0.230	5.6 ± 0.1	$3.23^{+0.82}_{-0.69}$	$3.95^{+3.00}_{-1.96}$
A383	0.188	4.1 ± 0.1	$3.11^{+0.88}_{-0.69}$	$5.59^{+6.31}_{-3.51}$
A520	0.203	7.9 ± 0.2	$4.20^{+2.30}_{-1.70}$	$2.20^{+1.10}_{-0.80}$
A521	0.248	6.1 ± 0.1	$4.58^{+1.00}_{-0.88}$	$2.18^{+1.13}_{-0.83}$
A586	0.171	$7.8^{+1.0}_{-0.8}$	$6.29^{+2.26}_{-1.69}$	$4.90^{+5.82}_{-3.16}$
A611	0.288	$7.1^{+0.6}_{-0.5}$	$5.47^{+1.31}_{-1.11}$	$3.01^{+1.99}_{-1.37}$
A697	0.282	$8.8^{+0.7}_{-0.6}$	$9.73^{+1.86}_{-1.61}$	$2.17^{+0.94}_{-0.73}$
A963	0.206	5.6 ± 0.1	$5.10^{+1.70}_{-1.40}$	2.10 ± 0.40
A1835	0.253	8.4 ± 0.1	$10.86^{+2.53}_{-2.08}$	$2.35^{+1.27}_{-0.93}$
A1914	0.171	8.5 ± 0.2	$4.20^{+2.90}_{-2.00}$	$3.20^{+0.70}_{-0.60}$
A2034	0.113	6.4 ± 0.2	$4.30^{+4.00}_{-2.40}$	$2.90^{+0.90}_{-0.70}$
A2219	0.228	$9.6^{+0.3}_{-0.2}$	$7.75^{+1.89}_{-1.60}$	$4.59^{+4.11}_{-2.53}$
A2261	0.224	$6.1^{+0.6}_{-0.5}$	$7.97^{+1.51}_{-1.31}$	$4.31^{+2.37}_{-1.72}$
A2390	0.231	9.1 ± 0.2	$6.92^{+1.50}_{-1.29}$	$4.40^{+2.63}_{-1.86}$
A2631	0.278	$7.5^{+0.4}_{-0.2}$	$4.54^{+0.89}_{-0.78}$	$5.57^{+4.24}_{-2.78}$
RX J1720	0.164	5.9 ± 0.1	$3.48^{+1.28}_{-0.99}$	$4.87^{+6.98}_{-3.45}$
RX J2129	0.235	5.6 ± 0.1	$5.29^{+1.76}_{-1.38}$	$4.67^{+6.21}_{-3.19}$
ZwCl 1454	0.258	4.6 ± 0.1	$2.80^{+1.39}_{-1.03}$	$2.18^{+3.25}_{-1.57}$
ZwCl 1459	0.290	6.4 ± 0.2	$3.77^{+1.17}_{-0.98}$	$4.10^{+4.56}_{-2.56}$

Notes: X-ray data from Planck Collaboration III (2013), Landry et al. (2013) and Kenneth et al. (2008).

We want to have all NFW profiles parametrized by M_{200} and c. In general, within a radius r_Δ, i.e. the scale for which the density is equal to Δ times the critical density, we have

$$\Delta = \frac{M_\Delta}{\frac{4}{3}\pi r_\Delta^3 \rho_c(z)}, \tag{24}$$

which results in an expression for the radius given the mass:

$$r_\Delta = \frac{1}{H(z)}\sqrt[3]{\frac{2\,G M_\Delta H(z)}{\Delta}}. \tag{25}$$

For the latter set of clusters, with NFW profiles specified by M_{500} and $c_{500} = \frac{r_{500}}{r_0}$ (rather than c_{200}, which we called just c), shown in Table 2, the parameter $r_0 = \frac{r_{200}}{c} = \frac{r_{500}}{c_{500}}$ comes immediately by using equation (25) for $\Delta = 500$. Using SYMPY in PYTHON, we get M_{200} and r_{200} by solving simultaneously an equation similar to equation (9) (but parametrized by M_{500} and c_{500} and evaluated at r_{200} to give M_{200}) and equation (25) with $\Delta = 200$

$$M_{200} = \frac{M_{500}}{\ln(1+c_{500}) - \frac{c_{500}}{1+c_{500}}} \times \left[\ln\left(1 + c_{500}\frac{r_{200}}{r_{500}}\right) - \frac{c_{500}\frac{r_{200}}{r_{500}}}{1 + c_{500}\frac{r_{200}}{r_{500}}}\right], \tag{26}$$

$$r_{200} = \frac{1}{H(z)}\sqrt[3]{\frac{G M_{200} H(z)}{100}}. \tag{27}$$

Then we can finally compute $c = \frac{r_{200}}{r_0}$.

For the former set, with NFW profiles specified by M_{200}, $M_{\rm vir}$ and $c_{\rm vir}$ (Table 1), 'vir' would correspond to some $\Delta_{\rm vir}$ around 200 but this value can vary with the redshift. Then we proceed as follows. We compute r_{200} from equation (25) and solve

$$M_{200} = \frac{M_{\rm vir}}{\ln(1+c_{\rm vir}) - \frac{c_{\rm vir}}{1+c_{\rm vir}}} \times \left[\ln\left(1 + c_{\rm vir}\frac{r_{200}}{r_{\rm vir}}\right) - \frac{c_{\rm vir}\frac{r_{200}}{r_{\rm vir}}}{1 + c_{\rm vir}\frac{r_{200}}{r_{\rm vir}}}\right] \tag{28}$$

for $r_{\rm vir}$. $\Delta_{\rm vir}$ can also be determined now with $r_{\rm vir}$ and $M_{\rm vir}$, inverting equation (25). Finally, we have $r_0 = \frac{r_{\rm vir}}{c_{\rm vir}}$ and $c = \frac{r_{200}}{r_0}$. The errors are estimated using a Monte Carlo method that we describe in the next section. With c and M_{200}, we can now proceed to the computation of the virial ratios.

3.2 Monte Carlo estimation of errors

We apply a Monte Carlo method to propagate uncertainties through the numerical solutions. We perform multiple realizations of each cluster, with the observables assuming values that are drawn from a distribution that reflects the 1σ confidence intervals from the original asymmetrical uncertainties. We then carry the computations for all the realizations of each cluster and analyse the final distribution of the quantities of interest to get their error bars.

3.2.1 *Uncertainties in M_{200} and c_{200}*

These two NFW parameters are always positive. In order to guarantee that their uncertainties will not lead to negative values in any of the random realizations, we choose the log-logistic distribution, a non-negative probability distribution that has simple analytical forms for its probability density function (PDF) and cumulative

distribution function (CDF). They are given, in terms of the parameters α and β, by

$$f_X(x;\alpha,\beta) = \frac{\frac{\beta}{\alpha}\left(\frac{x}{\alpha}\right)^{\beta-1}}{\left[1+\left(\frac{x}{\alpha}\right)^{\beta}\right]^2}, \quad F_X(x;\alpha,\beta) = \frac{1}{1+\left(\frac{x}{\alpha}\right)^{-\beta}}, \qquad (29)$$

respectively, for a random variable X.

Given an observable X with measured value $x^{+\Delta x_1}_{-\Delta x_2}$, we would like the Monte Carlo generating distribution to match the following criteria:

(i) the maximum probability coincides with the nominal measure;
(ii) the probability of X lying between $x - \Delta x_2$ and $x + \Delta x_1$ is 68 per cent;
(iii) the PDF has the same value at the two points $x - \Delta x_2$ and $x + \Delta x_1$, so that the interval in condition (ii) corresponds to the 68 per cent most probable values, i.e. 1σ C.L.

In the case of the log-logistic distribution, these conditions are translated by

(i) $\alpha(\frac{\beta-1}{\beta+1})^{1/\beta} = x$ (for $\beta > 1$);
(ii) $F_X(x+\Delta x_1;\alpha,\beta) - F_X(x-\Delta x_2;\alpha,\beta) = 0.68$;
(iii) $f_X(x-\Delta x_2;\alpha,\beta) = f_X(x+\Delta x_1;\alpha,\beta)$.

But these are too many conditions for a distribution that has only two parameters. We choose to relax condition (i) and solve (ii) and (iii) for α and β. In practice our resulting maximum probabilities usually happen to be very close to x.

When extracting the 1σ C.L., we take the opposite direction and get a best-fitting log-logistic PDF for the distributions of M_{200} and c, now solving (ii) and (iii) for $x - \Delta x_2$ and $x + \Delta x_1$. We assign the maximum probability of the distribution to the nominal value x.

We have also used the lognormal distribution to check whether our choice of distribution could be biasing our results. The lognormal PDF and CDF are given by

$$f_X(x;\mu,\sigma) = \frac{\mathrm{e}^{-(\ln x-\mu)^2/2\sigma^2}}{x\sigma\sqrt{2\pi}},$$
$$F_X(x;\mu,\sigma) = \frac{1}{2}\mathrm{erfc}\left[-\frac{\ln x-\mu}{\sigma\sqrt{2}}\right], \qquad (30)$$

where $\mathrm{erfc}(x)$ is the complementary error function and μ and σ are the Gaussian parameters of the distribution of $\ln X$.

We applied this Monte Carlo procedure for the clusters in our sample. However, the lognormal distribution could not satisfy our requirements (ii) and (iii) for all clusters in the first group. Nevertheless, we were able to verify in the other cases, where the lognormal distribution works, that the confidence intervals obtained with the two distributions are very similar, within a few per cent of displacement between their extremities. The maximum probability can vary a little more between the two distributions because (i) is not being satisfied, but we are more concerned with the confidence intervals, since we use uniform distributions for c, M_{200} and T_X in the evaluation of the virial ratios, interaction strength and departure from equilibrium. We believe, then, that the use of the log-logistic distribution with the requirements that we propose for the estimation of errors for M_{200} and c is a reasonable choice, as it works for all clusters and the results seem not to be biased.

3.2.2 *Virial ratios and interaction strength fittings*

In Table 3, we summarize the data used for computation of the virial ratios and interaction strengths according to the steps in Section 2.2. We assume flat distributions within the range $[x - \Delta x_2, x + \Delta x_1]$ for the inputs in the form $x^{+\Delta x_1}_{-\Delta x_2}$ in the generation of random realizations for our Monte Carlo method.

Inspection of the final distributions of virial ratios and interaction strengths suggests the use of lognormal distributions to fit (the negative of) the data. However, due to the nature of these quantities and their domains, we include a location parameter to allow the distribution to be shifted from the origin. The lognormal PDF is then

$$f_X(x;\mu,\sigma,x_{\rm loc}) = \frac{\mathrm{e}^{-[\ln(x-x_{\rm loc})-\mu]^2/2\sigma^2}}{(x-x_{\rm loc})\sigma\sqrt{2\pi}} \qquad (31)$$

with $x_{\rm loc}$ being the location parameter. We take the 68 per cent most probable values and the maximum probability of this lognormal PDF to yield the resulting value $x^{+\Delta x_1}_{-\Delta x_2}$ of the quantity X. The fits obtained are especially good for the interaction strengths, as we show in Section 4.2.

In addition, we introduce two selection criteria which we apply to the values of the interaction strength obtained with this method to conserve realizations: one physical, discussed in Section 2.1.1, selects $\xi \leq 3$, while the other avoids numerical problems, discussed in Section 2.1.2, by keeping only $\xi \geq -200$ (see discussion in Section 4.2).

3.2.3 *Reliability of the results*

Our analysis considers samples of 2600 random realizations of each cluster, but some of them happen to have no solution for ξ, or to have a solution outside the domain established by equation (3). These realizations are removed from the analysis, leading to considerably smaller samples for some clusters. That is the case for A68, A115, A520 and A1914, for which we are left with only about 200 realizations. A possible explanation for such a large fraction of these samples not having a physical solution for ξ could be linked with the dynamical activity of those clusters (e.g. Markevitch et al. 2005; Barrena, Girardi & Boschin 2013), so their virial states are not as close to equilibrium for our method to be applicable.

The gas distribution in clusters can be used as a probe of the recent past dynamical activity of a cluster, since the gas responds quickly to perturbations in the gravitational potential, for instance, due to cluster merger and/or collision (Andrade-Santos, Lima Neto & Laganá 2012). Visual inspections of *Chandra* X-ray images show that all clusters except A115, A520 and A1914 have rather undisturbed and symmetric gas distribution, suggesting that they are not dynamically active.

For comparison purposes, we define a 'success rate' (SR) as the fraction of realizations satisfying our selection criteria in the total generated for each cluster. Clusters like A1835, A209 and A2261 present this fraction very close or equal to 1. The SRs for all clusters are presented in Table 4. In the histograms, we use a number of bins proportional to the size of the samples.

In order to evaluate the consistency of our method, we consider a cluster from N-body simulation, similar to those of Machado & Lima Neto (2013), in a cosmology with $\Omega_{\rm M} = 0.3$, $\Omega_{\rm DE} = 0.7$, $h = 0.72$ and no interaction in the dark sector, so the virial ratio should

Table 4. Fraction of Monte Carlo-produced realizations for each cluster.

Cluster	A115	A1835	A1914	A2034	A209	A2219	A2261	A2390	A2631	A267	A383
SR	0.06	1.00	0.08	0.58	1.00	0.80	1.00	0.74	0.68	0.60	1.00
Cluster	A520	A521	A586	A611	A68	A697	A963	RX J1720	RX J2129	ZwCl 1454	ZwCl 1459
SR	0.05	0.67	0.85	0.80	0.11	0.98	0.91	0.72	1.00	0.64	0.63

Notes: The SR here presented were computed for our Monte Carlo samples of size 2600. Tests have shown that there is no significant variation of the SR with the size of the sample.

be very close[2] to -0.5 and interaction compatible with zero. The data for this cluster are $M_{200} = 18.0\,h^{-1}10^{14}\,\mathrm{M}_{\odot}$, $z = 0.0$, $c = 3.0$ and $T_X = 7.3 \pm 0.8$ keV. The uncertainty in the temperature comes from the σ_X–T_X scatter relation (Xue & Wu 2000)

$$\sigma_X = 10^{2.49\pm0.02} T_X^{0.65\pm0.03}, \tag{32}$$

from which T_X was computed for a one-dimensional velocity dispersion of $\sigma_X = 1125\,\mathrm{km\,s^{-1}}$. Because the observed virial ratio is linear with the temperature, the only source of errors in this case, its histogram for all random realizations produced in our code reflects clearly the uniform distribution assigned to the input temperature. Fitting that uniform distribution we find a virial ratio of -0.47 ± 0.04 from the central 68 per cent most probable values.

With the analysis of Section 3.2.2, for the interaction strength we get $\xi = -0.05^{+0.54}_{-0.69}$, therefore compatible with the simulation. The theoretical virial ratio (TVR) is also in accordance with the classic value, $(\frac{\rho_K}{\rho_W})_{th} = -0.51 \pm 0.05$, while the DfE being -0.08 ± 0.06 satisfies our condition (7).

4 ANALYSIS OF THE RESULTS

In what follows we discuss the outcome of our analysis starting with the observed virial ratios (hereafter OVR), their theoretical estimates (which we denote by TVR) from combining their DfE factors and their interaction strengths ξ. Throughout this section, we present the constraints on the virial ratios, interaction and departure from equilibrium in Figs 1(b), 2, 3 and 4, all obtained for each cluster according to the method described in the previous section. These results are summarized in Table 5. The detailed distributions of some of these quantities are shown in the Appendix A.

4.1 The observed virial ratios

The OVR is obtained from applying the method described in Section 3.2 to equation (14). The histograms of OVR produced for each cluster are very similar to what we obtain for their theoretical counterparts TVR (see Appendix A). As an example we present in Fig. 1(a) the distribution obtained for the cluster A2261. It represents the histogram distribution of the OVR obtained from our Monte Carlo sampling of mass, temperature and concentration ranges. Superimposed is the lognormal fit, with light-shaded area corresponding to 95 per cent C.L., and dark-shaded area emphasizing 68 per cent C.L. The red vertical line marks the theoretical non-interacting value, while the dashed line gives the most likely value.

We summarize the results of the OVR with their corresponding asymmetrical errors in Fig. 1(b), where we have shown the theoretical non-interacting virial ratio as a horizontal red line. We have ordered the clusters by increasing OVR and keep this order for the rest of the work.

[2] Some variations can be introduced by the effects of projection translating from simulation to observables.

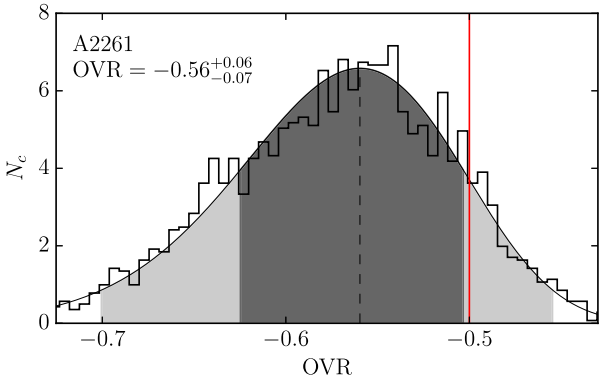

(a) OVR for the cluster A2261 from a sample of 2600 random realisations. $\frac{\rho_K}{\rho_W} = -0.56^{+0.06}_{-0.07}$.

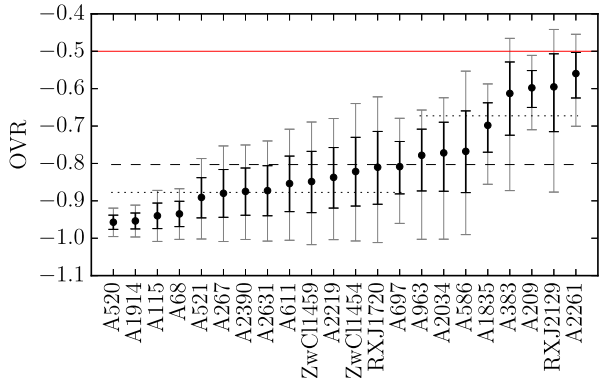

(b) OVR with error bars indicating 95% and 68% C.L. for all clusters.

Figure 1. Panel (a) shows in detail the distribution of the OVR for the cluster A2261 when we apply the Monte Carlo method (Section 3.2). N_c is the normalized count of Monte Carlo clusters per bin of OVR. The dark and light shaded areas correspond to 68 per cent and 95 per cent C.L. The dashed vertical line indicates the most probable value while the red solid line denotes the classic value. Panel (b) presents the most probable values and C.L.s for each cluster. The grey and black error bars give, respectively, the 95 per cent and 68 per cent C.L. The mean of the most probable values is signalled by the dashed black line. The two dotted lines show the means for the two groups of clusters defined in the text and the solid red line marks the classic value.

We have represented the mean value for the whole sample with a dashed line. We identify two groups of similar virial ratios separated by the global mean and for each group we represent their means by the dotted lines. The dispersion of the ratios may reflect the diversity of the equilibrium conditions. However, the first group seems to have less scatter than the second one.

With this robust non-linear treatment of error propagation, all clusters exclude -0.5 at 1σ.

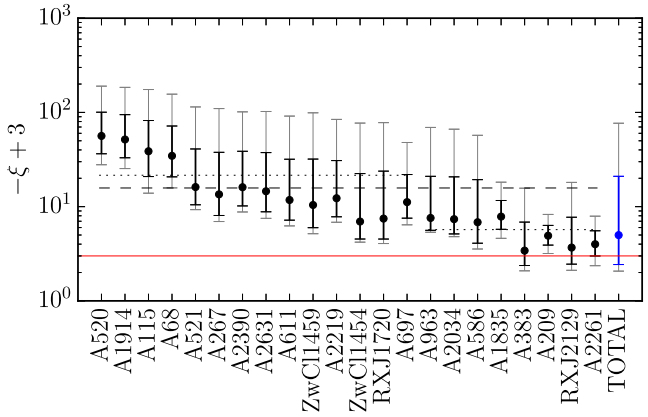

Figure 2. Interaction strengths with error bars for each cluster in our sample. The grey and black error bars give, respectively, the 95 per cent and 68 per cent C.L. The most probable value and error bars of the compounded distribution are shown at the right in blue. Again, dotted horizontal lines represent the means for each group of clusters, while the dashed line marks the overall mean. The solid red line marks $\xi = 0$. We plot $-\xi + 3$ rather than ξ to enable visualization in log scale.

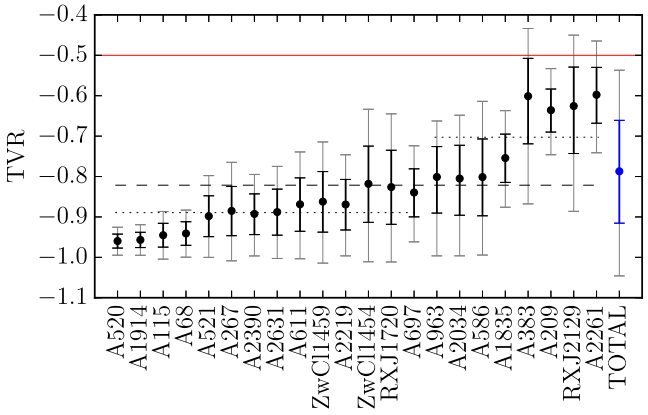

Figure 3. TVR with confidence intervals for each cluster in our sample and for the compounded distribution. Grey and black error bars give, respectively, 95 and 68 per cent C.L. The most probable value and error bars of the compounded distribution are shown at the right in blue. Dotted horizontal lines represent means for each group, while dashed line marks overall mean. The solid red line marks the non-interaction case.

4.2 The interaction strength

As previously mentioned we solve for ξ equation (6) with the departure from equilibrium term (22) using the Monte Carlo method of Section 3.2. Equation (8) is singular at $\frac{\rho_K}{\rho_W} = -1$, which corresponds to ξ infinite. This is a limitation of our method that we deal with by restricting the interaction strength to $|\xi| \leq 200$ such that the histograms would be legible. Note that this introduces a cut in the histograms of the TVR (Appendix A), which reflects the limitation of our method.

In Fig. 2, we plot the most probable value of $-\xi + 3$ for all clusters to keep the log scale, together with the 68 and 95 per cent C.L. corresponding to, respectively, black and grey error bars. The red solid line indicates the $\xi = 0$ absence of interaction. The mean value for the whole sample is given by the dashed line. Each group previously singled out also present their group mean as dotted lines. Finally, we add the most probable value and error bars of the compounded distribution in blue.

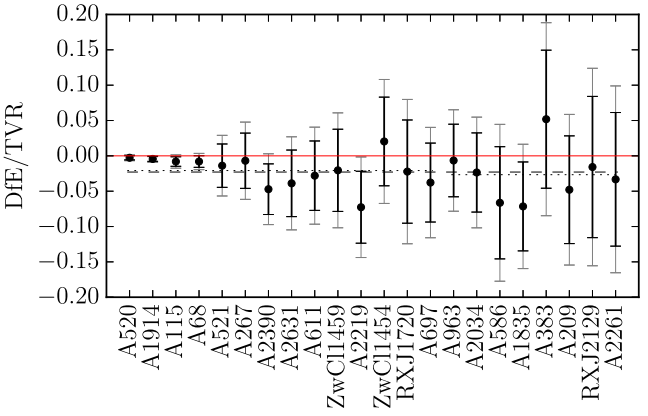

Figure 4. DfE factors relative to the TVR with confidence intervals for each cluster in our sample. Grey and black error bars give, respectively, 95 per cent and 68 per cent C.L. Dotted horizontal lines represent means for each group, while dashed line marks overall mean. The solid red line marks the absence of deviation.

Of the 22 clusters, all of them except A383, RX J2129 and A2261 (marginally) display a 1σ detection favouring negative ξ.

In this model, the interaction strength should be the same for all clusters. The global mean is compatible with 13 of the 22 clusters: A521, A267, A2390, A2631, A611, ZwCl 1459, A2219, ZwCl 1454, RX J1720, A697, A963, A2034, and A586. It gives -12.78. However, three of the clusters, as well as the compounded distribution that yields a value for $\xi = -1.99^{+2.56}_{-16.00}$, displays compatibility with no interaction. This points to problems in our method, namely when it assumed small deviation from equilibrium while the results have important variations. Actually, the lowest boundary is limited by the results of Salvatelli et al. (2013) to[3] -2.70 (see also Costa et al. 2014). Nevertheless, we concentrate on the present scheme and leave the solutions to a forthcoming work.

4.3 The theoretical virial ratios

Armed with the results from the previous section, we compute with equation (19) the TVR that each cluster would have at perfect equilibrium in the presence of interaction. Their corresponding distributions are shown in the Appendix A. As those histogram are very similar to the observed ones (Section 4.1), the following comments can be applied to both. The reasons for these similarities are discussed in Section 4.4. We plot in Fig. 3 the most probable values of TVR for all clusters, together with the 68 and 95 per cent C.L. corresponding to, respectively, black and grey error bars. The red solid line indicates the -0.5 classic virial value, in absence of interaction. The mean value for the whole sample is given by the dashed line. In the same way as with the interaction strengths, we compounded the distributions of the TVR for all the clusters, as they should all be equal to a universal value, and show the most probable value and its error bars in blue, at the right of the panel.

At this level, all the clusters exclude -0.5 at 1σ, which confirms the result from Section 4.1. However, 16 out of the 22 clusters present lognormal fits which reflects poorly the underlying distributions: A520, A1914, A115, A68, A521, A267, A2390, A2631, A611, ZwCl 1459, A2219, ZwCl 1454, RX J1720, A963, A2034 and A586 (see Appendix A). For all of those problematic distributions the lognormal fits break down for virial ratios in the proximity

[3] Salvatelli et al. have found $-2.70 < \xi < -0.66$ at 95 per cent C.L.

Table 5. Virial ratios, interactions, TVR and departure from equilibrium from the lognormal fits.

Cluster	OVR	ξ	TVR	DfE
A520	-0.96 ± 0.02	$-53.28^{+19.87}_{-44.20}$	-0.96 ± 0.02	-0.003 ± 0.003
A1914	-0.95 ± 0.02	$-48.60^{+18.59}_{-43.09}$	-0.96 ± 0.02	-0.004 ± 0.003
A115	-0.94 ± 0.03	$-35.72^{+17.85}_{-43.34}$	-0.95 ± 0.03	-0.01 ± 0.01
A68	-0.93 ± 0.03	$-31.62^{+13.90}_{-37.11}$	-0.94 ± 0.03	-0.01 ± 0.01
A521	-0.89 ± 0.05	$-13.14^{+5.67}_{-24.80}$	-0.90 ± 0.05	-0.01 ± 0.03
A267	-0.88 ± 0.06	$-10.50^{+5.45}_{-24.20}$	-0.89 ± 0.06	-0.01 ± 0.04
A2390	-0.87 ± 0.06	$-13.08^{+5.90}_{-22.60}$	-0.89 ± 0.05	-0.05 ± 0.04
A2631	-0.87 ± 0.07	$-11.56^{+5.75}_{-22.91}$	-0.89 ± 0.06	-0.04 ± 0.05
A611	$-0.85^{+0.07}_{-0.08}$	$-8.76^{+4.58}_{-20.08}$	-0.87 ± 0.07	-0.03 ± 0.05
ZwCl 1459	-0.85 ± 0.08	$-7.41^{+4.43}_{-21.56}$	$-0.86^{+0.07}_{-0.08}$	-0.02 ± 0.06
A2219	-0.84 ± 0.08	$-9.28^{+4.48}_{-18.55}$	-0.87 ± 0.06	-0.07 ± 0.05
ZwCl 1454	-0.82 ± 0.09	$-3.95^{+2.42}_{-15.49}$	$-0.82^{+0.09}_{-0.10}$	0.02 ± 0.06
RX J1720	-0.81 ± 0.10	$-4.47^{+2.94}_{-16.34}$	-0.83 ± 0.09	-0.02 ± 0.07
A697	-0.81 ± 0.07	$-8.17^{+3.62}_{-10.75}$	-0.84 ± 0.06	-0.04 ± 0.06
A963	$-0.78^{+0.07}_{-0.10}$	$-4.59^{+1.98}_{-13.39}$	$-0.80^{+0.08}_{-0.09}$	-0.01 ± 0.05
A2034	$-0.77^{+0.08}_{-0.10}$	$-4.37^{+2.23}_{-13.35}$	$-0.80^{+0.08}_{-0.09}$	-0.02 ± 0.06
A586	-0.77 ± 0.11	$-3.83^{+2.74}_{-12.51}$	$-0.80^{+0.09}_{-0.10}$	-0.07 ± 0.08
A1835	$-0.70^{+0.06}_{-0.07}$	$-4.84^{+2.10}_{-3.78}$	-0.75 ± 0.06	-0.07 ± 0.06
A383	$-0.61^{+0.08}_{-0.11}$	$-0.41^{+1.04}_{-3.44}$	$-0.60^{+0.09}_{-0.12}$	0.05 ± 0.10
A209	-0.60 ± 0.05	$-1.92^{+1.01}_{-1.41}$	-0.64 ± 0.05	-0.05 ± 0.08
RX J2129	$-0.60^{+0.09}_{-0.12}$	$-0.68^{+1.23}_{-4.04}$	$-0.63^{+0.10}_{-0.12}$	-0.02 ± 0.10
A2261	$-0.56^{+0.06}_{-0.07}$	$-0.99^{+1.00}_{-1.55}$	-0.60 ± 0.07	-0.03 ± 0.09
TOTAL	–	$-1.99^{+2.56}_{-16.00}$	-0.79 ± 0.13	–

of -1. This is related to the singularity in equation (8). In addition, the compounded TVR points towards a single value of -0.79 ± 0.13, which represents a detection at 2σ, in contradiction with the results of the previous section. All this suggests a problem with our method that assumed small deviation from equilibrium, as previously pointed out.

In the following section, we discuss how the observed and the TVR are so similar.

4.4 The departure from equilibrium factors

Equation (22) with the results of Section 4.2 allows us to compute the DfE factor for each cluster. The values of this factor relative to their TVR,

$$\frac{\mathrm{DfE}}{\mathrm{TVR}} = \frac{-\left(2-\frac{\xi}{3}\right)^{-2}\dot{\rho}_W/H\rho_W}{(\rho_K/\rho_W)_{\mathrm{th}}} = \frac{\dot{\rho}_W/H\rho_W}{(1-\xi/3)(2-\xi/3)}, \qquad (33)$$

are presented in Fig. 4. Except for A1914, A115, A2390, A2219, and A1835, all those relative departures appear compatible with zero. We should note as well that ZwCl 1454 and A383 are the only clusters with positive DfE. For this figure and for numerical reasons, we fit the distributions for each cluster with uniform distributions so as to evaluate the order of magnitude of those departures and produce the values displayed on Fig. 4. Although not good fits, these uniform distributions enable us to show how small those values are, validating our hypothesis (7). This explains the similarities between OVR and TVR, as seen in comparing Figs 1(b) and 3.

5 DISCUSSION AND CONCLUSIONS

We analysed the virial ratios of a set of clusters using a simple model based on the Layzer–Irvine equation (Bertolami et al. 2007; Le Delliou et al. 2007; Bertolami et al. 2008, 2009; Abdalla et al. 2009, 2010; He et al. 2010; Bertolami et al. 2012), using weak-lensing mass profiles and intracluster gas temperatures from optical and X-ray observations (Okabe et al. 2010; Planck Collaboration III 2013). Our treatment involved assessing the virial balance of each cluster as well as their equilibrium state, using a Monte Carlo statistical analysis on the data. Note that the equilibrium state evaluation should encompass every single known and unknown source of deviation from balance.

Our method, a first proof of concept for out of equilibrium virial evaluation, enabled us to find mild evidence for an interacting dark sector in the virial balance of those clusters, however yielding only small amplitudes of departure from equilibrium: although the compounded distribution of all clusters would accommodate $\xi = 0$, a majority of the individual clusters, of their virial ratios and of the compounded evaluation of the virial ratio all point towards a negative interaction. The compounded estimates give us $\xi = -1.99^{+2.56}_{-16.00}$, which is not a detection, but TVR $(\rho_K/\rho_W)_{\mathrm{th}} = -0.79 \pm 0.13$, which is a detection at 2σ. This tension between the compounded results for the interaction strength and the TVR, while the latter is constructed out of the former, points to the main problem in our results: despite the scatter in the values of virial ratios, the departure from equilibrium factors remain small, as imposed in our hypotheses. In addition, our method contains an unphysical singularity at $\frac{\rho_K}{\rho_W} = -1$ in equation (8). These problems, in spite of encouraging results, call for follow up work which should

remove the small departure from equilibrium hypothesis, as well as the singularity we introduced in this work for $\rho_K = -\rho_W$.

Most observed clusters appear to be somewhat perturbed systems and are maybe still forming (accreting mass), which is expected in the current standard cosmological scenario. Our approach, that treat clusters as out of equilibrium systems, is therefore natural, despite the measurement of such departure not following the observed wide variations in virial states. The tension between the results of our measured departure from the classic virial ratio and our measured interaction strength reflects both that our method shows potential but also has room for improvement and we can expect that accommodation for large departures should enable the use of much larger samples that can enhance statistically the significance of the results.

ACKNOWLEDGEMENTS

The work of M.Le D. has been supported by FAPESP (2011/24089-5) and PNPD/CAPES20132029. M.Le D. also wishes to acknowledge DFMA/IF/USP and IFT/UNESP. R.J.F.M. and G.B.L.N. thank CAPES for support. G.B.L.N. also wish to thank CNPq. E.A. acknowledges FAPESP. Finally, we thank Rubens Machado for his simulation.

REFERENCES

Abdalla E., Abramo L. R. W., Sodré L., Jr, Wang B., 2009, Phys. Lett. B, 673, 107
Abdalla E., Abramo L. R., de Souza J. C. C., 2010, Phys. Rev. D, 82, 023508
Amendola L., 2000, Phys. Rev. D, 62, 043511
Andrade-Santos F., Lima Neto G. B., Laganá T. F., 2012, ApJ, 746, 139
Armendariz-Picon C., Mukhanov V. F., Steinhardt P. J., 2001, Phys. Rev. D, 63, 103510
Baldi M., Pettorino V., Robbers G., Springel V., 2010, MNRAS, 403, 1684
Barrena R., Girardi M., Boschin W., 2013, MNRAS, 430, 3453
Bennett C. L. et al. (WMAP Collaboration), 2013, ApJS, 208, 20
Bento M. C., Bertolami O., Sen A. A., 2002, Phys. Rev. D, 66, 043507
Bertolami O., Gil Pedro F., Le Delliou M., 2007, Phys. Lett. B, 654, 165
Bertolami O., Gil Pedro F., Le Delliou M., 2008, EAS Publ. Ser., 30, 161
Bertolami O., Gil Pedro F., Le Delliou M., 2009, Gen. Relativ. Gravit., 41, 2839
Bertolami O., Gil Pedro F., Le Delliou M., 2012, Gen. Relativ. Gravit., 44, 1073
Bilić N., Tupper G. B., Viollier R. D., 2002, Phys. Lett. B, 535, 17
Binney J., Tremaine S., 2008, Galactic Dynamics. Princeton Univ. Press, Princeton, NJ
Caldwell R. R., Dave R., Steinhardt P. J., 1998, Phys. Rev. Lett., 80, 1582
Carlesi E., Knebe A., Lewis G. F., Yepes G., 2014, MNRAS, 439, 2958
Copeland E. J., Liddle A. R., Wands D., 1998, Phys. Rev. D, 57, 4686
Costa A. A., Xu X.-D., Wang B., Ferreira E. G. M., Abdalla E., 2014, Phys. Rev. D, 89, 103531
Ettori S., Donnarumma A., Pointecouteau E., Reiprich T. H., Giodini S., Lovisari L., Schmidt R. W., 2013, Space Sci. Rev., 177, 119
He J.-H., Wang B., Abdalla E., Pavon D., 2010, J. Cosmol. Astropart. Phys., 1012, 022
He J.-H., Wang B., Abdalla E., 2011, Phys. Rev. D, 83, 063515
Hinshaw G. et al. (WMAP Collaboration), 2013, ApJS, 208, 19
Kenneth W. C., Megan D., Voit G. M., Sun M., 2008, ApJ, 682, 821
Kravtsov A. V., Borgani S., 2012, ARA&A, 50, 353
Landry D., Bonamente M., Giles P., Maughan B., Joy M., Murray S., 2013, MNRAS, 433, 2790
Le Delliou M., Bertolami O., Gil Pedro F., 2007, in Rajantie A., Contaldi C., Dauncey P., Stoica H., ed., AIP Conf. Proc. Vol. 957, Particles, Strings, and Cosmology. Am. Inst. Phys.,New York, p. 421
Machado R. E. G., Lima Neto G. B., 2013, MNRAS, 430, 3249
Markevitch M., Govoni F., Brunetti G., Jerius D., 2005, ApJ, 627, 733
Moretti A., Gastaldello F., Ettori S., Molendi S., 2011, A&A, 528, A102
Navarro J. F., Frenk C. S., White S. D. M., 1996, ApJ, 462, 563
Okabe N., Masahiro T., Umetsu K., Futamase T., Smith G. P., 2010, PASJ, 62, 811
Peebles P. J. E., 1993, Principles of Physical Cosmology, Princeton Univ. Press, Princeton, NJ
Perlmutter S. et al., 1998, Nature, 391, 51
Pettorino V., 2013, Phys. Rev. D, 6, 063519
Pettorino V., Amendola L., Baccigalupi C., Quercellini C., 2012, Phys. Rev. D, 86 103507
Planck Collaboration I, 2014a, A&A, 571, A1
Planck Collaboration III, 2013, A&A, 550, A129
Planck Collaboration XVI, 2014b, A&A, 571, A16
Pratt G. W., Böhringer H., Croston J. H., Arnaud M., Borgani S., Finoguenov A., Temple R. F., 2007, A&A, 461, 71
Ratra B., Peebles P. J. E., 1988, Phys. Rev. D, 37, 3406
Salvatelli V., Marchini A., Lopez-Honorez L., Mena O., 2013, Phys. Rev. D, 88, 023531
Sympy Development Team, SymPy: Python Library for Symbolic Mathematics. Available at: http://www.sympy.org
Tocchini-Valentini D., Amendola L., 2002, Phys. Rev. D, 65, 063508
Vikhlinin A., Markevitch M., Murray S. S., Jones C., Forman W., Van Speybroeck L., 2005, ApJ, 628, 655
Weinberg S., 1989, Rev. Mod. Phys., 61, 1
Weinberg S., 2008, Cosmology. Oxford Univ. Press, Oxford
Wetterich C., 1988, Nucl. Phys. B, 302, 668
Xue Y.-J., Wu X.-P., 2000, ApJ, 538, 65
Zimdahl W., Pavón D., 2001, Phys. Lett. B, 521, 133
Zimdahl W., Pavón D., 2003, Gen. Relativ. Gravit., 35, 413
Zlatev I., Wang L. M., Steinhardt P. J., 1999, Phys. Rev. Lett., 82, 896
Zwicky F., 1933, Helv. Phys. Acta, 6, 110
Zwicky F., 1937, ApJ, 86, 217

APPENDIX A: HISTOGRAMS OF THE VIRIAL RATIOS AND INTERACTION STRENGTHS

In Figs A1 and A2 we show, respectively, the histograms of interaction strengths and TVR for all clusters, their lowest rightmost panels displaying the compounded distribution for all the studied clusters. We keep conventions of light and dark shaded areas representing 95 and 68 per cent C.L., the dashed line for the most probable value and the red solid line (when visible) to indicate absence of interaction.

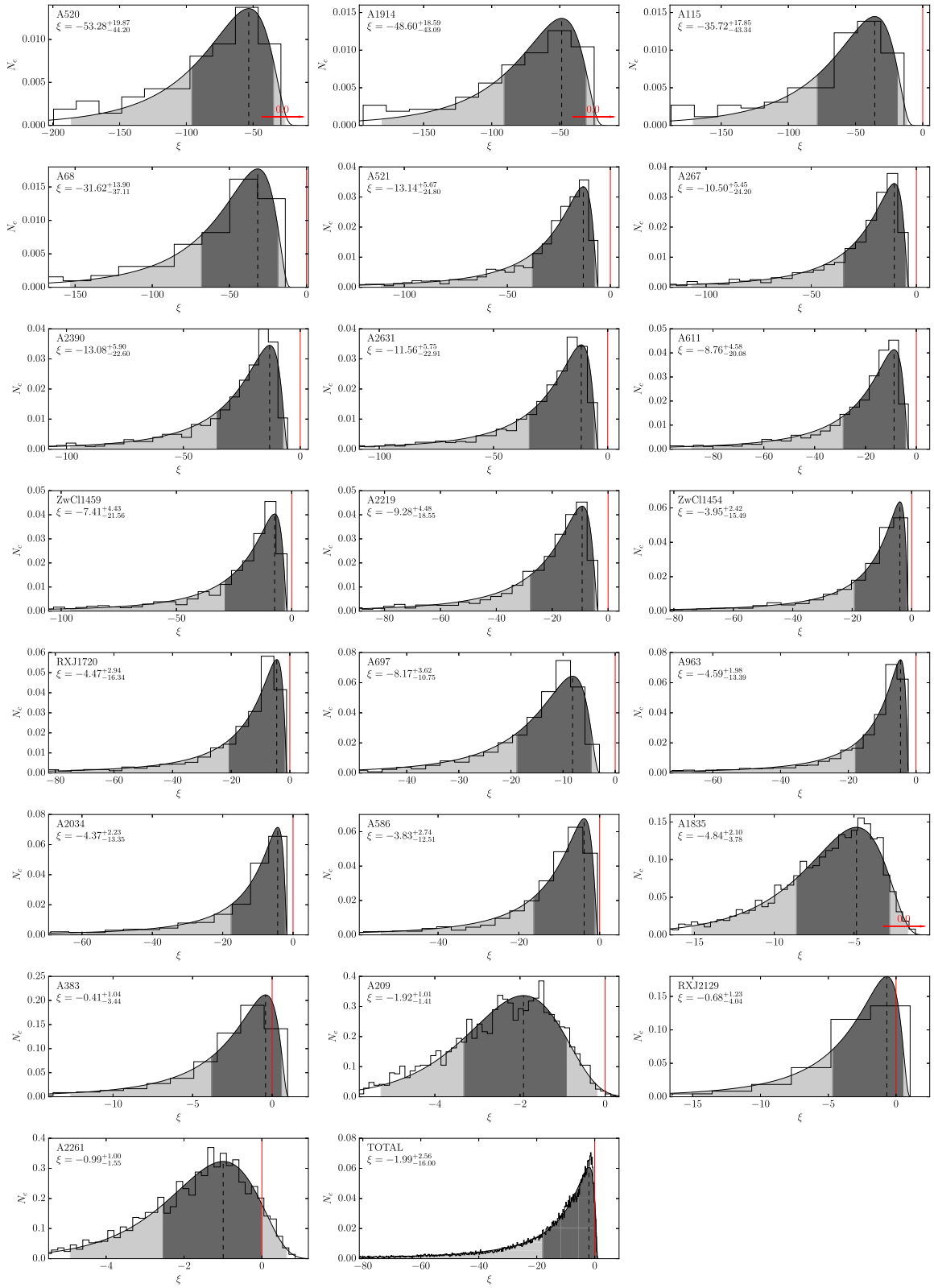

Figure A1. Histograms for the distributions of interaction strength ξ with their lognormal fits for each cluster. N_c is the normalized count of Monte Carlo clusters per bin of ξ. The lowest rightmost panel presents the cumulated histogram of all the clusters. The dark and light shaded areas mark the 68 and 95 per cent C.L. The dashed lines point the most probable values, indicated inside the frames with errors referring to the 68 per cent C.L., while the solid red line (red arrow) marks (points to) the $\xi = 0$ position.

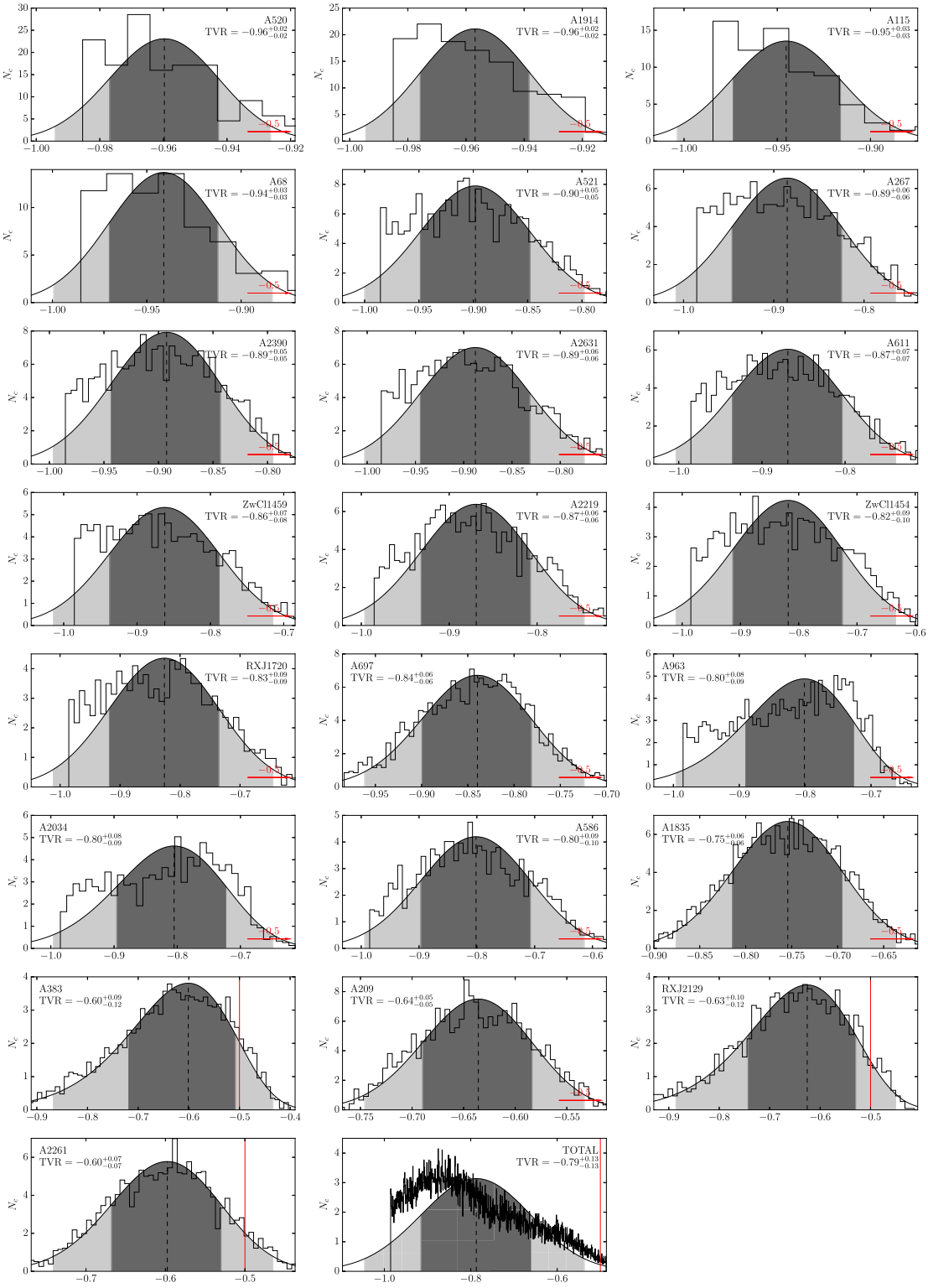

Figure A2. Histograms for the distributions of the TVR with their lognormal fits for each cluster. N_c is the normalized count of Monte Carlo clusters per bin of TVR. The lowest rightmost panel presents the cumulated histogram of all the clusters. The dark and light shaded areas mark the 68 and 95 per cent C.L. The dashed lines point the most probable values, indicated inside the frames with the errors referring to the 68 C.L., while the solid red line (red arrow) marks (points to) the position of the no interaction classic virial ratio.

This paper has been typeset from a TEX/LATEX file prepared by the author.